CrossMark

Calibrating the *Planck* Cluster Mass Scale with Cluster Velocity Dispersions

Stefania Amodeo[1], Simona Mei[1,2,3,4,5], Spencer A. Stanford[6,7], James G. Bartlett[3,8], Jean-Baptiste Melin[9], Charles R. Lawrence[3], Ranga-Ram Chary[5], Hyunjin Shim[10,5], Francine Marleau[11,5], and Daniel Stern[3]

[1] LERMA, Observatoire de Paris, PSL Research University, CNRS, Sorbonne Universités, UPMC Univ. Paris 06, F-75014 Paris, France
[2] Université Paris Denis Diderot, Université Paris Sorbonne Cité, F-75205 Paris Cedex 13, France
[3] Jet Propulsion Laboratory, California Institute of Technology, 4800 Oak Grove Drive, Pasadena, CA, USA
[4] Cahill Center for Astronomy & Astrophysics, California Institute of Technology, Pasadena, CA, 91125, USA
[5] Infrared Processing and Analysis Center, California Institute of Technology, Pasadena, CA, 91125, USA
[6] Department of Physics, University of California Davis, One Shields Avenue, Davis, CA 95616, USA
[7] Institute of Geophysics and Planetary Physics, Lawrence Livermore National Laboratory, Livermore, CA 94550, USA
[8] APC, AstroParticule et Cosmologie, Université Paris Diderot, CNRS/IN2P3, CEA/lrfu, Observatoire de Paris, Sorbonne Paris Cité, 10 rue Alice Domon et Léonie Duquet, F-75205, Paris Cedex 13, France
[9] DRF/Irfu/SPP, CEA-Saclay, F-91191, Gif-sur-Yvette Cedex, France
[10] Department of Earth Science Education, Kyungpook National University, Korea
[11] Institute of Astro and Particle Physics, University of Innsbruck, A-6020, Innsbruck, Austria

Abstract

We measure the *Planck* cluster mass bias using dynamical mass measurements based on velocity dispersions of a subsample of 17 *Planck*-detected clusters. The velocity dispersions were calculated using redshifts determined from spectra that were obtained at the Gemini observatory with the GMOS multi-object spectrograph. We correct our estimates for effects due to finite aperture, Eddington bias, and correlated scatter between velocity dispersion and the *Planck* mass proxy. The result for the mass bias parameter, $(1 - b)$, depends on the value of the galaxy velocity bias, $b_{\rm v}$, adopted from simulations: $(1 - b) = (0.51 \pm 0.09)b_{\rm v}^3$. Using a velocity bias of $b_{\rm v} = 1.08$ from Munari et al., we obtain $(1 - b) = 0.64 \pm 0.11$, i.e., an error of 17% on the mass bias measurement with 17 clusters. This mass bias value is consistent with most previous weak-lensing determinations. It lies within 1σ of the value that is needed to reconcile the *Planck* cluster counts with the *Planck* primary cosmic microwave background constraints. We emphasize that uncertainty in the velocity bias severely hampers the precision of the measurements of the mass bias using velocity dispersions. On the other hand, when we fix the *Planck* mass bias using the constraints from Penna–Lima et al., based on weak-lensing measurements, we obtain a positive velocity bias of $b_{\rm v} \gtrsim 0.9$ at 3σ.

Key words: cosmic background radiation – cosmology: observations – galaxies: clusters: general – galaxies: distances and redshifts

1. Introduction

Galaxy clusters are fundamental tools for tracing the evolution of cosmic structures and constraining cosmological parameters. Their number density at a given epoch is strongly dependent on the amplitude of density fluctuations, σ_8 (the standard deviation within a comoving sphere of radius $8\,h^{-1}$ Mpc), and the matter density of the Universe, $\Omega_{\rm m}$ (see, e.g., the review by Allen et al. 2011). The mass of galaxy clusters is a key quantity in their use as cosmological probes. Unfortunately, mass is not directly observable, but it can be estimated through several independent methods based on different physical properties that are each affected by their own set of specific systematic effects. Methods are based on the analysis of the thermal emission of the intracluster medium (ICM), observed either in the X-rays or through the Sunyaev–Zeldovich (SZ) effect (Sunyaev & Zeldovich 1970), the dynamics of member galaxies, and gravitational lensing. Comparison of mass estimates using different techniques is a critical check on the reliability of each method under different conditions, and also a test of the cosmological scenario.

The SZ effect originates from the transfer of energy from the heated electrons in the ICM to the photons of the cosmic microwave background (CMB) via inverse Compton scattering (see the review by Carlstrom et al. 2002). This scattering generates a distortion of the blackbody spectrum of the CMB, which appears as a decrease in intensity at frequencies below

218 GHz and as an increase in intensity at higher frequencies. The amplitude of this effect is quantified by the Compton parameter integrated along the line of sight, $y \propto T_{\rm e} n_{\rm e}$, where $T_{\rm e}$ and $n_{\rm e}$ are the electron temperature and density, respectively; or equivalently, is quantified by its solid-angle integral, $Y = \int y\, d\Omega$. Unlike optical or X-ray emission, the surface brightness of the SZ effect (relative to the mean CMB brightness) is independent of distance. Dedicated SZ cluster surveys can therefore efficiently find clusters out to high redshifts. Moreover, since the SZ signal is proportional to the thermal energy of the ICM, it can be used to estimate total cluster mass, and numerical simulations (e.g., Kravtsov et al. 2006) show that the integrated Compton signal, Y, tightly correlates with the mass.

Recent millimeter-wave surveys are providing large samples of SZ-detected clusters and applying them in cosmological analysis: the South Pole Telescope (SPT; Bleem et al. 2015; de Haan et al. 2016), the Atacama Cosmology Telescope (ACT; Marriage et al. 2011; Hasselfield et al. 2013), and the *Planck* satellite (Planck Collaboration et al. 2015). *Planck* produced two all-sky SZ cluster catalogs, the PSZ1 with 1227 detections based on 15.5 months of data, and the PSZ2 with 1653 detections from the full mission data set of 29 months (Planck Collaboration et al. 2014b, 2016b). Using subsamples of confirmed clusters at higher detection significance, *Planck* constrained cosmological parameters from the cluster counts (Planck Collaboration et al. 2014a, 2016a), noting tension with

the values of σ_8 and Ω_m favored by the primary CMB anisotropies.

The largest source of uncertainty in cosmological inference from the cluster counts is the SZ-signal–halo mass relation. Higher angular resolution SZ observations show that the *Planck* determination of the SZ signal is robust (Rodriguez-Gonzalvez et al. 2017; Sayers et al. 2016). *Planck* calibrates the relation with mass proxies from *XMM-Newton* X-ray observations (Arnaud et al. 2010); the proxies are in turn calibrated, assuming the hydrostatic equilibrium of the ICM (see the Appendix of Planck Collaboration et al. 2014a). This assumption, however, neglects possible contributions from bulk motions and non-thermal sources to the pressure support of the ICM. Analyses of mock data from simulations indicate that these can cause a 10%–25% underestimate of cluster total mass (e.g., Nagai et al. 2007; Piffaretti & Valdarnini 2008; Meneghetti et al. 2010). Other effects, such as instrument calibration or temperature inhomogeneities in the gas (Rasia et al. 2006, 2014), can additionally bias hydrostatic mass measurements. It is common to lump all possible astrophysical and observational biases into the mass bias parameter, $(1 - b)$, defined in Section 3. Simulations and comparison of different X-ray analyses indicate the range, $b = 0\%$–40%, with a baseline value of 20% (Mazzotta et al. 2004; Nagai et al. 2007; Piffaretti & Valdarnini 2008; Lau et al. 2009; Kay et al. 2012; Rasia et al. 2012; Rozo et al. 2014a, 2014b, 2014c). To reconcile the *Planck* cluster constraints with those of the primary CMB, a mass bias of $(1 - b) = 0.58 \pm 0.04$ is required (Planck Collaboration et al. 2016a). The comparison of *Planck* and CARMA-8 measurements by Rodriguez-Gonzalvez et al. (2017) shows that this tension is not due to any bias in the *Planck* flux measurements. Moreover, a recent analysis of the local X-ray cluster temperature function finds that the same mass bias value is needed to reconcile the X-ray cluster abundance with the CMB cosmology (Ilic et al. 2015).

Weak gravitational lensing (WL) provides an alternate method of measuring cluster mass (e.g., Hoekstra & Jain 2008). The bending of light by the cluster gravitational field distorts the images of background galaxies, elongating them tangentially around the cluster. Statistical analysis of such distortions gives a direct estimate of the density profile of the cluster and its total mass. Gravitational lensing is particularly efficient in estimating cluster mass because it is sensitive to the total mass, independently of cluster composition or dynamical state. However, since WL measures the projected mass, cluster triaxiality and the presence of substructures along the line of sight introduce significant noise; nevertheless, the noise can be reduced by stacking the WL signal from a large number of clusters to yield an unbiased estimate of the sample mass (Sheldon et al. 2004; Johnston et al. 2007; Corless & King 2009; Meneghetti et al. 2010; Becker & Kravtsov 2011).

Several recent WL calibrations of the *Planck* cluster scale have found results in the range of $0 < b < 30\%$, at the 10% precision level (von der Linden et al. 2014; Hoekstra et al. 2015; Simet et al. 2017a; Smith et al. 2016). Melin & Bartlett (2015) propose a new technique to measure cluster masses through lensing of CMB temperature anisotropies. First detections of this effect have been reported by Planck Collaboration et al. (2016b), Baxter et al. (2015) for SPT, and Madhavacheril et al. (2015) for ACT, which holds great promise for the future. Battaglia et al. (2016) have pointed out the potential impact of the Eddington bias—the steep mass function scattering the meaning is: the scatter is larger for low-mass objects more low-mass than high-mass objects into an SZ-signal bin—on these mass calibrations. Using a complete

Bayesian analysis to account for this and other effects, Penna-Lima et al. (2016) obtained a value of $b \sim 25\%$, which is consistent with previous measurements. This illustrates the importance of the cluster mass measurements and the need for independent determinations, as well as the need for increasing precision.

An additional, widely used method to constrain cluster mass takes the velocity dispersion of member galaxies as a measure of the gravitational potential of the dark-matter halo, which is assumed to be in virial equilibrium. The scaling relation between velocity dispersion and mass has been well established by cosmological *N*-body and hydrodynamical simulations (e.g., Evrard et al. 2008; Munari et al. 2013), which confirm the trend of $\sigma \propto M^{1/3}$ expected from the virial relation for a broad range of masses, redshift, and cosmological models. Cluster member galaxies may not, however, share the same velocity dispersion as the bulk of the dark matter, as they are hosted by subhalos whose dynamical states may differ. This introduces the concept of the velocity bias (e.g., Carlberg 1994; Colín et al. 2000) that mass estimates must be able to account for. Recently, Sifón et al (2016) presented dynamical mass estimates based on galaxy velocity dispersions for a sample of 44 clusters observed with ACT. Their sample spans a redshift range of $0.24 < z < 1.06$, with an average of 55 spectroscopic members per cluster. Comparing dynamical and SZ mass estimates, they find a mass bias of $(1 - b) = 1.10 \pm 0.13$ (i.e., $b = -10\%$).

In the present work, we study the relation between velocity dispersion and the SZ *Planck* mass for a sample of 17 *Planck* clusters observed at the Gemini Observatory to estimate the mass bias parameter. All but one cluster are in the PSZ2. In Section 2 we describe the observations and the sample, and then present our results in Section 3. We discuss the resulting mass bias measurement and compare our results to previous measurements in Section 4; we also turn the analysis around to constrain the velocity bias by adopting a constraint on the mass bias from WL observations. Section 5 concludes. Throughout, we adopt the *Planck* base ΛCDM model (Planck Collaboration et al. 2016b): a flat universe with $\Omega_m = 0.307$ and $H_0 = 67.74 \ \mathrm{km \, s^{-1} \, Mpc^{-1}}$ ($h \equiv H_0 / (100 \ \mathrm{km \, s^{-1} \, Mpc^{-1}})$). Mass measurements are quoted at a radius of R_Δ, within which the cluster density is Δ times the critical density of the universe at the cluster's redshift, where $\Delta = \{200, 500\}$. All quoted uncertainties are at a 68.3% (1σ) confidence level, unless otherwise stated.

2. The Data Set

2.1. Gemini/GMOS Spectroscopy

The goal of our program was to obtain an independent statistical calibration of the *Planck* SZ mass estimator. We chose *Planck* SZ-selected clusters that were detected with a signal-to-noise of 4.5σ or larger, distributed in the north and in the south, with a broad range in mass. We obtained pre-imaging and optical spectroscopy with GMOS-N and GMOS-S at the Gemini-North and Gemini-South Telescopes (Programs GN-2011A-Q-119, GN-2011B-Q-41, and GS-2012A-Q-77; P.I. J.G. Bartlett), respectively, of 19 galaxy clusters, spanning a range of $2 \times 10^{14} \, M_\odot \lesssim M_{500,\mathrm{SZ}} \lesssim 10^{15} \, M_\odot$ in *Planck* SZ masses (a more detailed discussion of these observations will follow in a companion paper). We were able to obtain velocity dispersion measurements for 17 clusters, which constitute our sample in this paper. All but one (PLCK G183.33-36.69) are in the PSZ2 catalog.

The northern sample was selected in the SDSS (Sloan Digital Sky Survey (SDSS); York et al. 2000) area. We used the SDSS

Table 1
The Cluster Sample Used in This Paper

Name	R.A. (deg)	Decl. (deg)	Im. Filter	t_{exp} (s)	N_{mask}	Run
PSZ2 G033.83−46.57	326.3015	−18.7159	g, i	1800	2	GS-2012A-Q-77
PSZ2 G053.44−36.25	323.8006	−1.0493	r	1800	1	GN-2011A-Q-119,GN-2011B-Q-41
PSZ2 G056.93−55.08	340.8359	−9.5890	r	1800	2	GN-2011A-Q-119,GN-2011B-Q-41
PSZ2 G081.00−50.93	347.9013	3.6439	r	1800		GN-2011A-Q-119,GN-2011B-Q-41
PSZ2 G083.29−31.03	337.1406	20.6211	r	1800		GN-2011A-Q-119,GN-2011B-Q-41
PSZ2 G108.71−47.75	3.0715	14.0191	r	1800	2	GN-2011A-Q-119,GN-2011B-Q-41
PSZ2 G139.62+24.18	95.4529	74.7014	r	900	2	GN-2011A-Q-119,GN-2011B-Q-41
			g, i, r, J, K			Palomar Hale Telescope
PSZ2 G157.43+30.34	117.2243	59.6974	r	3600	2	GN-2011A-Q-119,GN-2011B-Q-41
			g, i, r, J, K			Palomar Hale Telescope
PLCK G183.33−36.69	57.2461	4.5872	r	1800	2	GN-2011A-Q-119,GN-2011B-Q-41
			g, J, K			Palomar Hale Telescope
PSZ2 G186.99+38.65	132.5314	36.0717	r	1800	2	GN-2011A-Q-119,GN-2011B-Q-41
PSZ2 G216.62+47.00	147.4658	17.1196	r	1800	2	GN-2011A-Q-119,GN-2011B-Q-41
PSZ2 G235.56+23.29	134.0251	−7.7207	g, i	900	2	GS-2012A-Q-77
PSZ2 G250.04+24.14	143.0626	−17.6481	g, i	1800		GS-2012A-Q-77
PSZ2 G251.13−78.15	24.0779	−34.0014	g, i	900	2	GS-2012A-Q-77
PSZ2 G272.85+48.79	173.2938	−9.4812	g, i	900	2	GS-2012A-Q-77
PSZ2 G329.48−22.67	278.2527	−65.5555	g, i	900	2	GS-2012A-Q-77
PSZ2 G348.43−25.50	291.2293	−49.4483	g, i	900	2	GS-2012A-Q-77

Note. We list the PSZ2 cluster ID, when available. When it is not available, we use the prefix "PLCK" followed by a notation in galactic coordinates similar to that used in the PSZ2 paper.

public releases and GMOS-N pre-imaging in the r-band for 150 s to detect red galaxy overdensities at the *Planck* detection, and, when unknown, estimate the approximate redshift using their red sequence. For PSZ2 G139.62+24.18 and PSZ2 G157.43+30.34, we used imaging obtained with the Palomar telescope (PI: C. Lawrence). For the Southern sample, we obtained GMOS-S imaging in the g- and i-bands for 200 s and 90 s, respectively. Red galaxy overdensities and cluster members were selected by their colors using Bruzual & Charlot (2003) stellar population models and Mei et al. (2009) empirical red sequence measurements. In Table 1, we list our sample properties and the spectroscopy observing times.

The GMOS spectra were reduced using the tasks in the IRAF Gemini GMOS package and standard longslit techniques. After co-adding the reduced exposures, one-dimensional spectra for the objects in each slitlet were extracted and inspected visually to identify optical features such as the 4000 Å break, G-band, Ca H+K absorption lines, and, rarely, [O II]λ3727. More precise redshifts were determined by running the IRAF xcsao task on these spectra. We calculate the cluster velocity dispersions using the ROSTAT software (Beers et al. 1990) with both the Gaussian and biweight methods, which are appropriate for our clusters where there are typically 10–20 confirmed members. We retain cluster members galaxies within 3σ of the average cluster redshift. From the original sample of 19 clusters, we have excluded 2, which have complex non-Gaussian velocity distribution profiles. In a companion paper (S. Amodeo et al. 2017, in preparation), we show the velocity histograms of all observed clusters and publish catalogs of spectroscopic redshift measurements.

An important assumption that we make for this analysis is that our cluster sample is a representative, random subsample of the *Planck* SZ-selected catalog. In this case there are no corrections for selection effects, such as Malmquist bias, because we determine the mean scaling for the velocity dispersion given the SZ mass proxy.

2.2. Planck Mass Proxy

The *Planck* SZ mass proxy is based on a combination of *Planck* data and an X-ray scaling relation established with *XMM-Newton*. It has been used in the last two *Planck* cluster catalog papers (Planck Collaboration et al. 2014b, 2016b). Here we give a brief summary and refer the reader to section 7.2.2 of Planck Collaboration et al. (2014b) for more details.

With respect to the PSZ2, in this paper we derive new cluster mass estimates, taking into account the cluster centers from our Gemini/Palomar optical follow-up. For each cluster, we measure the SZ flux, Y_{500}, inside a sphere of radius of R_{500} using the Multifrequency Matched Filter (MMF3, Melin et al. 2006). The filter combines the six highest frequency bands (100–857 GHz) weighted to optimally extract a signal with the known SZ spectral shape and with an assumed spatial profile. For the latter, we adopt the so-called universal pressure profile from Arnaud et al. (2010). We center the filter on the optical position and vary its angular extent, θ_{500}, over the range of [0.9–35] arcmin to map out the signal-to-noise surface over the flux-size (Y_{500}–θ_{500}) plane. In the *Planck* data there is a degeneracy between the measured flux and cluster size defined by this procedure, which we break using an X-ray determined scaling relation as a prior constraint (i.e., an independent $Y - \theta$ relation obtained from the combination of Equations (7) and (9) of Planck Collaboration et al. 2014a). The intersection of the former with that of the *Planck* degeneracy contours yields a tighter constraint on the flux Y_{500}, which we then convert to halo mass, M_{500}^{Pl}, using Equation (7) of Planck Collaboration et al. (2014a). It is important to note that the mass proxy is therefore calibrated on the *XMM-Newton* scaling relation. These masses are reported in Table 2. In order to compare our mass measurements to those of the other independent estimates, we rescale the *Planck* masses to M_{200}^{Pl} using the mass–concentration relation of Dutton & Macciò (2014). The

Table 2
Redshifts, Velocity Dispersions, and SZ Masses

Name	z	N_{gal}	R_{max} (R_{200})	R_{200} (Mpc)	$\sigma_{1D}\,(<R_{max})$ (km s^{-1})	σ_{200} (km s^{-1})	M_{200}^{Pl} ($10^{14}\,M_\odot$)	M_{500}^{Pl} ($10^{14}\,M_\odot$)
PSZ2 G033.83−46.57	0.439	10	0.58	1.66 ± 0.08	985^{+451}_{-277}	953^{+454}_{-282}	7.8 ± 1.1	$5.4^{+0.7}_{-0.8}$
PSZ2 G053.44−36.25	0.331	20	0.42	1.93 ± 0.06	1011^{+242}_{-131}	956^{+260}_{-161}	10.9 ± 1.0	$7.5^{+0.5}_{-0.6}$
PSZ2 G056.93−55.08	0.443	46	0.49	2.00 ± 0.05	1356^{+192}_{-127}	1290^{+218}_{-164}	13.8 ± 1.1	9.4 ± 0.5
PSZ2 G081.00−50.93	0.303	15	0.41	1.88 ± 0.06	1292^{+360}_{-185}	1220^{+381}_{-223}	9.8 ± 0.9	6.7 ± 0.5
PSZ2 G083.29−31.03	0.412	20	0.49	1.89 ± 0.06	1434^{+574}_{-320}	1365^{+584}_{-338}	11.3 ± 1.0	$7.8^{+0.5}_{-0.6}$
PSZ2 G108.71−47.75	0.390	10	0.55	1.65 ± 0.08	900^{+458}_{-190}	865^{+461}_{-198}	7.3 ± 1.1	$5.1^{+0.7}_{-0.8}$
PSZ2 G139.62+24.18	0.268	20	0.36	1.96 ± 0.06	1120^{+366}_{-238}	1052^{+390}_{-273}	10.6 ± 0.9	7.3 ± 0.5
PSZ2 G157.43+30.34	0.402	28	0.47	1.94 ± 0.05	1244^{+192}_{-109}	1182^{+216}_{-148}	12.1 ± 1.0	8.2 ± 0.6
CL G183.33−36.69	0.163	11	0.35	1.38 ± 0.17	897^{+437}_{-275}	842^{+451}_{-297}	3.3 ± 1.2	$2.3^{+0.7}_{-0.9}$
PSZ2 G186.99+38.65	0.377	41	0.49	1.81 ± 0.06	1506^{+164}_{-120}	1432^{+200}_{-166}	9.5 ± 1.0	$6.6^{+0.6}_{-0.7}$
PSZ2 G216.62+47.00	0.385	37	0.45	1.97 ± 0.05	1546^{+174}_{-132}	1466^{+218}_{-186}	12.3 ± 1.0	$8.4^{+0.5}_{-0.6}$
PSZ2 G235.56+23.29	0.374	23	0.51	1.73 ± 0.08	1644^{+285}_{-192}	1568^{+308}_{-224}	8.2 ± 1.2	$5.7^{+0.7}_{-0.8}$
PSZ2 G250.04+24.14	0.411	29	0.53	1.75 ± 0.07	1065^{+447}_{-285}	1020^{+452}_{-293}	8.9 ± 1.0	6.2 ± 0.6
PSZ2 G251.13−78.15	0.304	9	0.48	1.59 ± 0.08	801^{+852}_{-493}	762^{+854}_{-497}	5.9 ± 0.9	4.1 ± 0.6
PSZ2 G272.85+48.79	0.420	10	0.57	1.65 ± 0.08	1462^{+389}_{-216}	1411^{+397}_{-231}	7.6 ± 1.1	$5.3^{+0.7}_{-0.8}$
PSZ2 G329.48−22.67	0.249	11	0.38	1.73 ± 0.07	835^{+179}_{-119}	786^{+200}_{-149}	7.2 ± 0.9	$5.0^{+0.5}_{-0.6}$
PSZ2 G348.43−25.50	0.265	20	0.37	1.84 ± 0.06	1065^{+411}_{-198}	1003^{+427}_{-230}	8.7 ± 0.9	6.0 ± 0.6

Note. From left to right the columns list the Cluster ID, our measured average redshift, the number of confirmed member galaxies, the maximum radius probed by GMOS, R_{max}, R_{200}, our measured velocity dispersion, $\sigma\,(<R_{max})$, the velocity dispersion estimated within R_{200}, σ_{200}, the reference PSZ2 M_{500}^{Pl}, and the M_{200}^{Pl} derived in this work based on SZ.

Table 3
Best-fit Values and Vertical Scatter (i.e., at Given Mass) of the Velocity Dispersion–Mass Relation, $\sigma = A\,[E(z)M/10^{15}\,M_\odot]^B$, Together with Mass Bias Estimates

Relation	A (km s^{-1})	B	Scatter $\langle\delta_{\ln\sigma}^2\rangle^{1/2}$	$(1-b)/b_v^3 f_{EB} f_{corr}$	$(1-b)_{Munari}$[a]
All clusters					
$\sigma_{1D}\,(<R_{max})$–M_{200}^{Pl}	1239 ± 99	0.29 ± 0.21	0.189 ± 0.018	⋯	⋯
$\sigma_{1D}\,(<R_{max})$–M_{200}^{Pl}	1226 ± 68	1/3	0.182 ± 0.012	0.47 ± 0.08	0.55 ± 0.09
σ_{200}–M_{200}^{Pl}	1172 ± 93	0.28 ± 0.20	0.198 ± 0.018	⋯	⋯
σ_{200}–M_{200}^{Pl}	1158 ± 61	1/3	0.189 ± 0.009	0.55 ± 0.09	0.64 ± 0.11
Only clusters with $N_{gal} \geqslant 20$					
$\sigma_{1D}\,(<R_{max})$–M_{200}^{Pl}	1250 ± 71	1/3	0.168 ± 0.014	0.44 ± 0.08	0.51 ± 0.09
σ_{200}–M_{200}^{Pl}	1156 ± 58	1/3	0.136 ± 0.012	0.56 ± 0.08	0.66 ± 0.09

Notes. Results are given for our velocity dispersion estimates, $\sigma_{1D}\,(<R_{max})$, and for the derived velocity dispersions within R_{200}, σ_{200}. We distinguish the case where all clusters in the sample are included in the fit from the case where only those with at least 20 member galaxies are considered.
[a] The values of the mass bias quoted in the last column are obtained using the velocity bias, b_v, derived by Munari et al. (2013), following the notation of Equation (5), where the Eddington bias correction is also included.

rescaling procedure is described in Appendix A and the resulting values of M_{200}^{Pl} are listed in Table 2.

2.3. Correcting Velocity Dispersions for GMOS Finite Aperture

The GMOS spectrographs provide imaging and spectroscopy over a 5.5 × 5.5 arcmin^2 field of view, allowing measurements for only the central part of clusters. The radial coverage provided for each cluster at a given redshift, calculated for the *Planck* 2015 cosmology, is quoted in Table 2 as R_{max} in units of R_{200}, along with R_{200}. We typically sample out to about half R_{200}, with R_{max} ranging over $[0.35–0.58]R_{200}$. However, we need to estimate the velocity dispersion within

R_{200}, $\sigma_{200} \equiv \sigma\,(<R_{200})$ to compare to the σ–M relation from the simulations (see the next section). Sifón et al. (2016) determine the radial profile of the velocity dispersion using mock observations of subhalos in the Multidark simulation (Prada et al. 2012), as described in Section 3.2 of their paper. We interpolate the correction factors presented in their Table 3 to our values of R_{max}/R_{200} to translate our velocity dispersion measurements, $\sigma_{1D}\,(<R_{max})$, to σ_{200}. Thus, the estimated velocity dispersions are listed in Table 2, where the uncertainties account for our measurement errors and the scatter in the velocity dispersion profile found by Sifón et al. (2016). The mean corrections are of the order of 5%, while the uncertainty increases up to 32%. Figure 1 plots the velocity dispersions σ_{200} versus M_{200}^{Pl}.
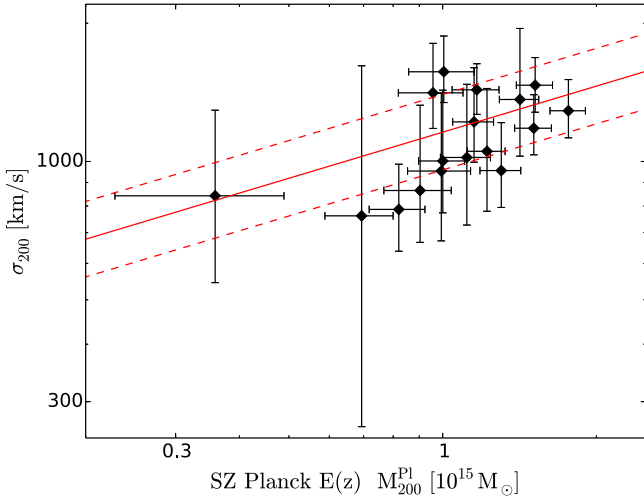
Figure 1. Relation between the *Planck* SZ mass proxy and velocity dispersion for our sample of 17 galaxy clusters observed with Gemini (diamonds). The velocity dispersions and the *Planck* masses have been converted to σ_{200} and M_{200}^{Pl}, respectively, with corresponding uncertainties following the procedure described in the text. The solid red line shows the best fit to the functional form of Equation (2) in log-space, where the slope is set to $1/3$, with the dashed lines delineating the dispersion of the data about the best-fit line.

3. Analysis: The Mass Bias

3.1. The Mass Bias and the Velocity Bias

Our goal is to find the *Planck* cluster mass scale using velocity dispersion as an independent mass proxy calibrated on numerical simulations. We define the mass bias factor, $(1 - b)$, in terms of the ratio between the *Planck*-determined mass, M_{200}^{Pl}, and true cluster mass, M_{200} (von der Linden et al. 2014; Hoekstra et al. 2015; Planck Collaboration et al. 2016b). We assume that mass bias factor is a constant and independent of overdensity. In fact, while the mass bias may depend on the mass and other cluster properties, our small sample only permits us to constrain a characteristic value averaged over the sample. For M_{200}, the mass bias is defined as

$$M_{200}^{\mathrm{Pl}} = (1 - b)M_{200}. \tag{1}$$

Complete virialization predicts a power-law relation between velocity dispersion, σ_{200}, and mass, M_{200}. Following the approach used in the simulations, we work with the logarithm of these quantities, $s_{\mathrm{v}} = \ln(\sigma_{200}/\mathrm{km\,s^{-1}})$, $\mu = \ln(E(z)M_{200}/10^{15}\,M_{\odot})$, where $h(z) \equiv H(z)/(100\ \mathrm{km\,s^{-1}\,Mpc^{-1}}) = hE(z)$ is the dimensionless Hubble parameter at redshift z, and we consider the log-linear relation of

$$\langle s_{\mathrm{v}}|\mu\rangle = a_{\mathrm{d}} + \alpha_{\mathrm{d}}\mu. \tag{2}$$

The so-called self-similar slope that is expected from purely gravitational effects is $\alpha_{\mathrm{d}} = 1/3$. The angle brackets indicate that this is the mean value of s_{v}, given μ. From a suite of simulations, Evrard et al. (2008) determined a precise relation between the dark-matter velocity dispersion and the halo mass that was consistent with this expectation. They find a normalization of $a_{\mathrm{d}} = \ln(1082.9 \pm 4.0) + \alpha_{\mathrm{d}} \ln h$; in the following, we will also refer to $A_{\mathrm{d}} \equiv e^{a_{\mathrm{d}}}$. The result is insensitive to cosmology and to nonradiative baryonic effects, and the relation is very tight, with only 4% scatter at fixed mass.

Galaxies, however, may have a different velocity dispersion than their dark-matter hosts because they inhabit special locations within the cluster, e.g., subhalos. This leads to the concept of velocity bias, in which the scaling of galaxy velocity dispersion with host halo mass will, in general, be fit by a relation of the form of Equation (2), but with different parameters, $A_{\mathrm{g}} \equiv e^{a_{\mathrm{g}}}$ and α_{g}. Simulations typically find the exponent α_{g} to be consistent with the self-similar value of $1/3$, so we can quantify any velocity bias in terms of the normalization, A_{g}. We do so by introducing the velocity bias parameter of $b_{\mathrm{v}} \equiv A_{\mathrm{g}}/A_{\mathrm{d}}$.

Different simulation-based or empirical analyses find discordant behavior for the velocity bias, leaving the sense of the effect (i.e., $b_{\mathrm{v}} > 1$ or $b_{\mathrm{v}} < 1$) up for debate.

Using hydrodynamical simulations with star formation, gas cooling and heating by supernova explosions, and AGN feedback, Munari et al. (2013) found that subhalos and galaxies have a slightly higher velocity dispersion than that of the dark matter, i.e., a positive velocity bias with $b_{\mathrm{v}} > 1$. For galaxies in their AGN-feedback model, for example, they find $A_{\mathrm{g}} = 1177$, corresponding to $b_{\mathrm{v}} = 1.08$.

From combined *N*-body and hydrodynamical simulations, Wu et al. (2013) found that velocity bias depends on the tracer population, in particular, that subhalos in pure *N*-body simulations tend to have large positive bias compared to galaxies identified in the hydrodynamical simulations, perhaps because over-merging in the former case removes slower, low-mass dark-matter halos from the tracer population. Consistent with this notion where smaller objects are more efficiently destroyed, all tracers in their simulations show increasingly positive velocity bias with decreasing subhalo mass or galaxy luminosity, independent of redshift. The brightest cluster galaxies tend to underestimate the dark-matter halo velocity dispersion, while faint galaxies slightly overestimate the dark-matter halo velocity dispersion, with the velocity bias ranging from ∼0.9 for the five brightest cluster galaxies to an asymptotic value of $b_{\mathrm{v}} = 1.07$ when including the 100 brightest galaxies (see Figure 1 in their paper). For samples of more than ∼50 galaxies, their result converges to the value of Munari et al. (2013; $b_{\mathrm{v}} = 1.08$). The 10–20 brightest galaxies, similar to our observational sample, represent a nearly unbiased measurement of the halo velocity dispersion, i.e., $b_{\mathrm{v}} = 1$.

On the other hand, Guo et al. (2015) observe the opposite trend with luminosity when measuring the velocity bias of galaxies in the SDSS Data Release 7 (see their Figure 9). They find $b_{\mathrm{v}} \simeq 1.1$ for the brightest galaxies, falling to 0.85 for faint galaxies. It is worth noting that this analysis is based on modeling of the projected and redshift-space two-point correlation functions, and it is probably not very sensitive to velocity bias in the most massive halos, such as those in the *Planck* sample. Farahi et al. (2016) use the velocity bias from the bright subsample of Guo et al. (2015) ($b_{\mathrm{v}} = 1.05 \pm 0.08$) to estimate the mass of redMaPPer clusters with stacked galaxy velocity dispersions. Their derived mass scale is consistent with the estimates based on weak-lensing observations reported by Simet et al. (2017b). The Guo et al. (2015) observational result is also consistent with the value $b_{\mathrm{v}} = 1.08$ from the *N*-body hydrodynamical simulations of Munari et al. (2013). In an another study, Caldwell et al. (2016) find a negative velocity bias, $b_{\mathrm{v}} = 0.896$, for galaxies in their simulations when they adjust feedback efficiencies to reproduce the present-day stellar mass function and the hot-gas fraction of clusters and groups.

These different studies do not yet present a clear picture of the magnitude of cluster member velocity bias, and this quantity remains the primary factor limiting interpretation of dynamical cluster mass measurements at present. We use the

Munari et al. value of the velocity bias, $b_v = 1.08$, as our baseline in the following. The uncertainty on Munari et al.'s velocity bias is $\sim 0.6\%$.

3.2. Measurement of the Mass Bias

As detailed in Appendix B, our model of constant mass bias, $(1 - b)$, predicts a log-linear scaling relation of the form of Equation (2) between the observed velocity dispersion and the *Planck* mass proxy. We therefore construct an estimator for $(1 - b)$ by fitting for the normalization, a, and exponent, α, of this relation to the data in Figure 1. We perform the fit using the MPFIT routine in IDL (Markwardt 2009; Williams et al. 2010) and taking into account only the uncertainties in the velocity dispersion (i.e., at fixed *Planck* SZ mass[12]).

For a robust estimation of the best-fit parameters, we perform 1000 bootstrap resamplings of the pairs $(M_{200}^{\mathrm{Pl}}, \sigma_{200})$, re-computing the best-fit parameters each time. This yields $A \equiv e^a = (1172 \pm 93)$, and a slope of $\alpha = 0.28 \pm 0.20$ (at 68.3% confidence). The slope is consistent with the self-similar expectation of $\alpha = 1/3$, although with large uncertainty. We henceforth set $\alpha = 1/3$ and refit to find $A = (1158 \pm 61)$. The dispersion of the velocity measurements about the best-fit line (i.e., at given M_{200}^{Pl}) is $\langle \delta_{\ln \sigma}^2 \rangle^{1/2} = 0.189 \pm 0.009$. The best fit together with the data is plotted in Figure 1. A model with a zero slope is excluded at $\sim 2\sigma$ confidence, using the χ^2 difference (the χ^2 for the best-fit model is 12.2, the χ^2 for the zero-slope model is 14.3). We also performed the fit using only clusters with more than 20 member galaxies. Once again fixing $\alpha = 1/3$, we find that $A = (1156 \pm 58)$, in this case, consistent with the previous value.

Our estimator for the mass bias then follows from the formalism of Appendix B (Equation (23)),

$$(1 - b) = \left(\frac{A_g}{A}\right)^3 f_{\mathrm{EB}} f_{\mathrm{corr}} = \left(\frac{A_d}{A}\right)^3 b_v^3 f_{\mathrm{EB}} f_{\mathrm{corr}}, \qquad (3)$$

where f_{EB} (Equation (24)) is the Eddington bias correction and f_{corr} (Equation (25)) is a correction for correlated scatter between velocity dispersion and the *Planck* mass proxy. With our value for the normalization fit to the data and the value for dark matter from Evrard et al. (2008), we have numerically,

$$(1 - b) = (0.55 \pm 0.09) b_v^3 f_{\mathrm{EB}} f_{\mathrm{corr}}. \qquad (4)$$

In the next two subsections, we propose $f_{\mathrm{EB}} = 0.93 \pm 0.01$ and $f_{\mathrm{corr}} \approx 1.01$ as reference values. Our final value for the mass bias also depends on the cube of the velocity bias. Adopting our baseline of $b_v = 1.08$ from Munari et al. (2013), we have

$$(1 - b) = (0.64 \pm 0.11) \left(\frac{f_{\mathrm{corr}}}{1.01}\right). \qquad (5)$$

The quoted uncertainty accounts for measurement error, uncertainty on the Eddington bias correction, and uncertainty on the velocity bias given by Munari et al. (2013); it is dominated by the measurement error. The uncertainty on Munari et al.'s velocity bias ($\sim 0.6\%$) is a negligible contribution to our total error budget. It is more difficult to assign an uncertainty to the correction for correlated scatter, as this depends on the details of cluster physics; we argue below

---

[12] Taking into account errors on both velocity and mass measurements does not noticeably change the result.

that feedback makes this a minor correction, as reflected in our fiducial value of $f_{\mathrm{corr}} = 1.01$.

A summary of best-fit parameters for several velocity dispersion–mass relations is provided in Table 3. Where the slope is set to $1/3$, we quote our estimates of the *Planck* mass bias for the velocity bias derived by Munari et al. (2013), $b_v = 1.08$. We distinguish results for the full sample from results for the subsample of clusters with at least 20 member galaxies.

Our value of $(1 - b) = 0.64 \pm 0.11$ lies within 1σ of the value $(1 - b) = 0.58 \pm 0.04$ needed to reconcile the cluster counts with the primary CMB constraints.

3.3. Eddington Bias

In this section, we detail our Eddington bias correction. The Eddington bias correction (Equation (24)),

$$f_{\mathrm{EB}} = e^{-\beta \Sigma_{s_{\mathrm{Pl}}}^2}, \qquad (6)$$

depends on the local slope of the mass function on cluster scales, $\beta \approx 3$, and the total dispersion, $\Sigma_{s_{\mathrm{Pl}}}$, of the *Planck* mass proxy at a fixed true mass. This is because we assume that our sample is a random draw from the parent sample selected on M_{200}^{Pl}. As described in Section 2.2, the mass proxy is calculated as an intersection of *Planck* SZ measurements and the X-ray based scaling relation in Planck Collaboration et al. (2014a). We characterize the measurement uncertainty on M_{200}^{Pl} by averaging the calculated uncertainty over our cluster sample, $\sigma_{s_{\mathrm{Pl}}} = 0.13 \pm 0.02$. To estimate the intrinsic scatter, we convert the 0.17 ± 0.02 dispersion of the $Y - M^{5/3}$ relation (Planck Collaboration et al. 2014a) to $\tilde{\sigma}_{s_{\mathrm{Pl}}} = (3/5)(0.17 \pm 0.02) = 0.10 \pm 0.01$. Combining the two, we arrive at a total scatter of

$$\Sigma_{s_{\mathrm{Pl}}} = 0.16 \pm 0.02. \qquad (7)$$

Setting $\beta = 3$, we calculate an Eddington bias correction of

$$\ln f_{\mathrm{EB}} = -0.08(1 \pm 0.19), \qquad (8)$$

or a reference value of $f_{\mathrm{EB}} = 0.93(1 \pm 0.01) = 0.93 \pm 0.01$.

Our estimate for the intrinsic scatter in the *Planck* mass from Planck Collaboration et al. (2014a) may be optimistic. If we allow a value 50% larger, we get a correction of $f_{\mathrm{EB}} = 0.84 \pm 0.027$. The resulting mass bias would be $(1 - b) = (0.58 \pm 0.097)(f_{\mathrm{corr}}/1.01)$.

3.4. Correlated Scatter

The second correction to our mass bias estimator arises from correlated scatter between velocity dispersion and the *Planck* mass proxy. It is given by (Equation (25)),

$$f_{\mathrm{corr}} = e^{3\tilde{r}\beta \tilde{\sigma}_{s_v} \tilde{\sigma}_{s_{\mathrm{Pl}}}}, \qquad (9)$$

because only the intrinsic scatter is correlated. Stanek et al. (2010) examined the covariance between different cluster observables using the Millennium Gas Simulations (Hartley et al. 2008). They found significant intrinsic correlation between velocity dispersion and SZ signal, $\tilde{r} = 0.54$, in the simulation with only gravitational heating. In the simulation that additionally included cooling and pre-heating, however, the correlation dropped to $\tilde{r} = 0.079$. This would seem to make sense, as we might expect nongravitational physics, such as feedback and cooling, to decouple the SZ signal, which

measures the total thermal energy of the gas from the collisionless component.

While the scatter of the dark-matter velocity dispersion is only 4%, Munari et al. (2013) find a scatter in the range 0.1–0.15 for their subhalos and galaxies. Fixing $\beta = 3$ and taking $\tilde{r} = 0.08$, $\tilde{\sigma}_{s_v} = 0.15$, and $\tilde{\sigma}_{s_{Pl}} = (3/5)0.17 = 0.10$ as reference values, we have

$$\ln f_{corr} = 0.010 \left(\frac{\tilde{r}}{0.08}\right)\left(\frac{\tilde{\sigma}_{s_v}}{0.15}\right)\left(\frac{\tilde{\sigma}_{s_{Pl}}}{0.10}\right), \tag{10}$$

or a reference value of $f_{corr} = 1.01$.

4. Discussion

We have estimated the *Planck* cluster mass bias parameter by measuring the velocity dispersion of 17 SZ-selected clusters observed with Gemini. It is corrected for both Eddington bias and possible correlated scatter between velocity dispersion and the SZ mass proxy. These corrections are based on a multivariate log-normal model for the cluster observables that is detailed in Appendix B. We do not correct individual cluster masses for Eddington bias (e.g., Sifón et al. 2016), but rather apply a global correction to the mean scaling relation between velocity dispersion and *Planck* mass proxy.

Our primary objective in calibrating the mass bias of *Planck* clusters is to inform the cosmological interpretation of the *Planck* cluster counts. Planck Collaboration et al. (2014a) and Planck Collaboration et al. (2016a) found tension between the observed cluster counts and the counts predicted by the base ΛCDM model fit to the primary CMB anisotropies, with the counts preferring lower values of the power spectrum normalization, σ_8. The importance of the tension, however, depends on the normalization of the SZ signal–mass scaling relation. The *Planck* team uses a relation calibrated on *XMM-Newton* observations of clusters (see the Appendix of Planck Collaboration et al. 2014a), and proposed that the mass bias parameter, b, accounts for possible systematic offsets in this calibration due to astrophysics and (X-ray) instrument calibration. No offset corresponds to $b = 0$, while the value needed to reconcile the observed cluster counts with the base ΛCDM model is $(1 - b) = 0.58 \pm 0.04$ (Planck Collaboration et al. 2016a).

The possible tension between clusters and primary CMB has motivated a number of recent studies of the cluster mass bias in both X-ray and SZ catalogs (e.g., Sifón et al. 2013, 2016; Ruel et al. 2014; Battaglia et al. 2016; Bocquet et al. 2015; Simet et al. 2017a; Smith et al. 2016). For a like-to-like comparison, we focus here on determinations for the *Planck* clusters.

Rines et al. (2016) compare SZ and dynamical mass estimates of 123 clusters from the *Planck* SZ catalog in the redshift range of $0.05 < z < 0.3$. They use optical spectroscopy from the Hectospec Cluster Survey (Rines et al. 2013) and the Cluster Infall Regions in the SDSS project (Rines & Diaferio 2006), observing a velocity dispersion–SZ mass relation that is in good agreement with the virial scaling relation of dark-matter particles. They find neither significant bias of the SZ masses compared to the dynamical masses nor any evidence of large galaxy velocity bias. They conclude that the mass calibration of *Planck* clusters cannot solve the CMB–SZ tension and another explanation, such as massive neutrinos, is required.

von der Linden et al. (2014) examine 22 clusters from the Weighing the Giants (WtG) project that are also used in the

Planck cluster count cosmology analysis. Applying a weak-lensing analysis, they derive considerably larger masses than *Planck*, measuring an average mass ratio of $\langle M_{Planck}/M_{WtG} \rangle = 0.688 \pm 0.072$ with decreasing values for larger *Planck* masses. They claim a mass-dependent calibration problem, possibly due to the fact that the X-ray hydrostatic measurements used to calibrate the *Planck* cluster masses rely on a temperature-dependent calibration. A similar result is obtained by Hoekstra et al. (2015) based on a weak-lensing analysis of 50 clusters from the Canadian Cluster Comparison Project (CCCP). For the clusters detected by *Planck*, they find a bias of $0.76 \pm 0.05(stat) \pm 0.06(syst)$, with the uncertainty in the determination of photometric redshifts being the largest source of systematic error. Planck Collaboration et al. (2016a) used these latter two measurements as priors in their analysis of the SZ cluster counts. They also employed a novel technique based on CMB lensing (Melin & Bartlett 2015) to find $1/(1 - b) = 0.99 \pm 0.19$ when averaged over the full cluster cosmology sample of more than 400 clusters. As later pointed out by Battaglia et al. (2016), these constraints should be corrected for Eddington bias.[13]

Smith et al. (2016) use three sets of independent mass measurements to study the departures from hydrostatic equilibrium in the Local Cluster Substructure Survey (LoCuSS) sample of 50 clusters at $0.15 < z < 0.3$. The mass measurements comprise weak-lensing masses (Ziparo et al. 2016; Okabe & Smith 2016), direct measurements of hydrostatic masses using X-ray observations (Martino et al. 2014), and estimated hydrostatic masses from Planck Collaboration et al. (2016b). They found agreement between the X-ray-based and *Planck*-based tests of hydrostatic equilibrium, with an X-ray bias of 0.95 ± 0.05 and an SZ bias of 0.95 ± 0.04.

Finally, Penna-Lima et al. (2016) used lensing mass measurements from the Cluster Lensing And Supernova (CLASH, Postman et al. 2012) survey with Hubble to find a *Planck* mass bias of $(1 - b) = 0.73 \pm 0.10$. Employing a Bayesian analysis, they modeled the CLASH selection function and astrophysical effects, such as scatter in lensing and SZ masses and their potential correlated scatter, as well as possible bias in the lensing measurements. Their quoted uncertainty accounts for these effects by marginalizing over the associated nuisance parameters. They also provide a summary of recent mass calibration measurements, including the Eddington bias correction proposed by Battaglia et al. (2016) for the WtG and CCCP determinations. Sereno et al. (2017) found a result similar to Penna–Lima for the *Planck* mass bias, $(1 - b) = 0.76 \pm 0.08$, using weak-lensing masses from the Canada–France–Hawaii Telescope Lensing Survey (CFHTLenS; Heymans et al. 2012) and the Red Cluster Sequence Lensing Survey (RCSLenS; Hildebrandt et al. 2016).

Comparing to the values above, our result is ~30% lower (at ~2.5σ) than both the Smith et al. (2016) lensing determination and the Rines et al. (2016) determination, also based on velocity dispersions; both determinations favor little or no mass bias. However, we agree within 1σ with the results from WtG (von der Linden et al. 2014), the CCCP (Hoekstra et al. 2015),

---

[13] There is some confusion in the nature of these corrections. Battaglia et al. (2016) propose a correction for WtG and CCCP that is really more akin to a Malmquist bias, i.e., due to selection effects arising from the fact that some clusters in the WtG and CCCP samples do not have *Planck* mass proxy measurements.

and the CLASH (Postman et al. 2012) analysis by Penna-Lima et al. (2016).

If we use our value of $(1 - b) = (0.58 \pm 0.097)(f_{\rm corr}/1.01)$, obtained with 50% larger intrinsic scatter on *Planck* masses (see Section 3.3), it would still agree within 2σ with the results from weak lensing cited above. In both cases, our value of the mass bias is within 1σ of the value $(1 - b) = (0.58 \pm 0.04)$ needed to reconcile the cluster counts with the primary CMB.

4.1. Estimating the Velocity Bias $b_{\rm v}$ Using a Prior on the Mass Bias

Given the large differences in the velocity bias as predicted by simulations, it is worth turning the vice—the strong dependence of our mass calibration on velocity bias—into a virtue. Relying on accurate mass estimates provided by weak-lensing analyses, we derive a constraint on $b_{\rm v}$ from our measured velocity dispersions. We adopt the *Planck* mass calibration obtained by Penna-Lima et al. (2016), based on the lensing mass measurements from the Cluster Lensing And Supernova survey with Hubble (CLASH). Using a Bayesian analysis of CLASH mass measurements and *Planck* SZ measurements, they marginalize over nuisance parameters describing the cluster scaling relations and the sample selection function to obtain $(1 - b) = 0.73 \pm 0.10$. This is a reasonable prior, since the Penna-Lima et al. (2016) sample is characteristic in mass (and we also assume in mass bias) of *Planck*-detected clusters. Using this as a prior on the mass bias in Equation (4), with our reference value for the Eddington bias given in Section 3.3, we then deduce the constraint to be

$$b_{\rm v} = 1.12 \pm 0.07 \left(\frac{1.01}{f_{\rm corr}} \right)^{1/3}. \qquad (11)$$

This positive velocity bias agrees with the value from the Munari et al. (2013) simulations and the Guo et al. (2015) result for samples more luminous than $M_{\rm r} = 20.5$ ($L_\star$). It is reasonably consistent (within 2σ) with the results of Wu et al. (2013) that predict nearly unbiased velocities for the brightest 10–30 galaxies that are appropriate for our sample. Our result is discrepant, at 3σ, with a negative velocity bias of $b_v \lesssim 0.9$, as found, for example, by the Caldwell et al. (2016) simulations.

5. Conclusions

We have examined the *Planck* cluster mass bias using a sample of 17 *Planck* clusters for which we measured velocity dispersions with GMOS at the Gemini observatory. The unknown velocity bias, $b_{\rm v}$, of the member galaxy population, is the largest source of uncertainty in our final result, $(1 - b) = (0.51 \pm 0.09)b_{\rm v}^3$. Using our baseline value for $b_{\rm v}$ from Munari et al. (2013), we find $(1 - b) = (0.64 \pm 0.11)$, consistent within just over 1σ with WtG, CCCP, and CLASH, and within 1σ of the value $(1 - b) = (0.58 \pm 0.04)$ needed to reconcile the *Planck* cluster counts with the primary CMB.

We conclude that velocity bias is the primary factor limiting interpretation of dynamical cluster mass measurements at this time. It is essential to eliminate this modeling uncertainty if velocity dispersion is to be a robust mass determination method.

Turning the analysis around, observational constraints on the velocity bias can be obtained by combining accurate mass estimates from weak-lensing measurements with velocity dispersion measurements. Assuming a prior on the mass bias from Penna-Lima et al. (2016), we derive $b_{\rm v} = 1.12 \pm 0.07$, consistent with our baseline value from Munari et al. (2013; $b_{\rm v} = 1.08$) and with results from Wu et al. (2013) and Guo et al. (2015), but discrepant at 3σ, with a negative velocity bias of $b_{\rm v} \lesssim 0.9$, as found by Caldwell et al. (2016).

Apart from modeling uncertainty on the velocity bias, we have achieved a precision of 17% on the mass bias measurement with 17 clusters. Assuming that the simulations will eventually settle on a value for the velocity bias, this motivates continued effort to increase our sample size to produce a 10% or better determination, comparable to recent weak-lensing measurements.

Appendix A
Conversion from $M_{500}^{\rm Pl}$ to $M_{200}^{\rm Pl}$

To compare our mass measurements to other independent estimates, we rescale the *Planck* masses to $M_{200}^{\rm Pl}$ using the mass–concentration relation of Dutton & Macciò (2014). This relation is derived from *N*-body simulations of relaxed dark-matter halos in a *Planck* cosmology, as adopted here. It is in good agreement with the recently proposed universal model of Diemer & Kravtsov (2015), which includes both relaxed and unrelaxed halos, for the mass and redshift range of interest.

We assume a Navarro–Frenk–White (NFW, Navarro et al. 1997) density profile, and we choose an input value for the concentration $c_{200} = 5$, which is consistent with the model of Dutton & Macciò (2014) for a $10^{15} h^{-1} M_\odot$ cluster in the redshift range of $0 < z < 0.5$. We then convert $M_{500}^{\rm Pl}$ to

$$M_{200}^{\rm Pl} = M_{500}^{\rm Pl} \frac{f(c_{200})}{f(c_{500})}, \qquad (12)$$

where $f(c_\Delta) = \log(1 + c_\Delta) - \frac{c_\Delta}{1+c_\Delta}$ indicates a general density contrast. We calculate c_{500} from

$$M_{500}^{\text{Pl}} = 4\pi\rho_s r_s^3 f(c_{500}), \tag{13}$$

where c_{500} is the only unknown quantity, because the scale density parameter, ρ_s, is fixed by the NFW profile,

$$\rho_s = \rho_{c,z} \frac{200}{3} \frac{c_{200}^3}{\ln(1 + c_{200}) - \frac{c_{200}}{1+c_{200}}}, \tag{14}$$

and the scale radius is

$$r_s = \frac{R_{500}}{c_{500}}, \tag{15}$$

with

$$R_{500} = \left[M_{500}^{\text{Pl}} \frac{3}{4\pi} \frac{1}{500} \frac{1}{\rho_{c,z}} \right]^{1/3}. \tag{16}$$

We solve Equation (13) for c_{500} using the ZBRENT.PRO routine in IDL and obtain a first estimate of M_{200}^{Pl} from Equation (12). We then use the mass–concentration relation in Equation (8) of Dutton & Macciò (2014) to get a new value for c_{200}. We iterate this algorithm until we reach 5% accuracy on M_{200}^{Pl} (i.e., the difference between the mass estimated at the iteration i and the mass estimated at the iteration i-1 is less than 0.05). We find smaller concentrations than the starting value of 5, with a mean $c_{200} = 4.2$. We have verified that the algorithm converges to the same values of M_{200}^{Pl} when changing the initial input value of c_{200}.

We implemented this procedure in a Monte Carlo simulation with 1000 inputs for each cluster, sampling the *Planck* mass, M_{500}^{Pl}, according to a normal distribution with a standard deviation taken as the geometric mean of the uncertainties listed in Table 2. Similarly, we consider a log-normal distribution for c_{200} with a mean given by Equation (8) in Dutton & Macciò (2014) and standard deviation equal to the intrinsic scatter of 0.11 dex in the mass–concentration relation. This yields a log-normal distribution of calculated M_{200}^{Pl} values from Equation (12), whose mean and standard deviation are also listed in Table 2.

Appendix B
Cluster Model

To construct an estimator for the mass bias, we adopt a multivariate log-normal model for the cluster observables σ_{1D} and M_{200}^{Pl} at fixed true mass, M_{200}, following White et al. (2010) and Stanek et al. (2010; see also, Allen et al. 2011; Evrard et al. 2014; Rozo et al. 2014b). It is then convenient to work with the logarithm of these quantities: $s_v = \ln(\sigma_{1D}/\text{km s}^{-1})$, $s_{\text{Pl}} = \ln(E(z)M_{200}^{\text{Pl}}/10^{15} M_\odot)$, and $\mu = \ln(E(z)M_{200}/10^{15} M_\odot)$, where we incorporate self-similar evolution with redshift, $E(z)$, with the masses. Power-law scaling relations give the observable mean values at true mass as,

$$\bar{s}_{\text{Pl}} \equiv \langle s_{\text{Pl}}|\mu\rangle = \ln(1 - b) + \mu, \tag{17}$$

and

$$\bar{s}_v \equiv \langle s_v|\mu\rangle = a_v + \alpha_v \mu, \tag{18}$$

where the averages are taken over both intrinsic cluster properties and measurement errors. The first relation is simply

our definition of the mass bias, Equation (1), and in practice we take $\alpha_v = 1/3$, its self-similar value, in the second relation.

Each observable is also associated with a log-normal dispersion about its mean that includes both intrinsic and measurement scatter,

$$\Sigma_{s_v}^2 = \tilde{\sigma}_{s_v}^2 + \sigma_{s_v}^2, \tag{19}$$

and

$$\Sigma_{s_{\text{Pl}}}^2 = \tilde{\sigma}_{s_{\text{Pl}}}^2 + \sigma_{s_{\text{Pl}}}^2, \tag{20}$$

where the first terms are the intrinsic log-normal scatter and the second ones are the measurement error. Although measurement error is Gaussian in the observed quantity rather than in the log-normal, we treat its fractional value as a log-normal dispersion; this is an approximation that is good to first order in the fractional measurement error. The second terms in the above expressions will therefore be understood as fractional measurement errors. The intrinsic dispersions may be correlated with the correlation coefficient $\tilde{r} = \langle(s_v - \bar{s}_v)(s_{\text{Pl}} - \bar{s}_{\text{Pl}})\rangle / (\tilde{\sigma}_{s_v}\tilde{\sigma}_{s_{\text{Pl}}})$.

It is then possible to show that the predicted scaling between velocity dispersion and *Planck* mass is

$$\langle s_v|s_{\text{Pl}}\rangle = a_v + \alpha_v [s_{\text{Pl}} - \ln(1 - b) - \beta\Sigma_{s_{\text{Pl}}}^2 + r\beta\alpha_v^{-1}\Sigma_{s_v}\Sigma_{s_{\text{Pl}}}], \tag{21}$$

where β is the slope of the mass function on cluster scales, $\beta \approx 3$. The second to last term is the Eddington bias, proportional to the full dispersion, intrinsic, and measurement, in the sample selection observable, s_{Pl}. In the last term, $r = \tilde{r}(\tilde{\sigma}_{s_v}/\Sigma_{s_v})(\tilde{\sigma}_{s_{\text{Pl}}}/\Sigma_{s_{\text{Pl}}})$, the intrinsic correlation coefficient is diluted by the measurement errors. The last term is therefore equivalent to $\tilde{r}\beta\alpha_v^{-1}\tilde{\sigma}_{s_v}\tilde{\sigma}_{s_{\text{Pl}}}$.

This is the prediction for our measured scaling relation. Comparison to our fit identifies

$$\ln A = a_v - \alpha_v [\ln(1 - b) + \beta\Sigma_{s_{\text{Pl}}}^2 - \tilde{r}\beta\alpha_v^{-1}\tilde{\sigma}_{s_v}\tilde{\sigma}_{s_{\text{Pl}}}], \tag{22}$$

which leads to our estimator

$$(1 - b) = \left(\frac{A_g}{A}\right)^3 f_{\text{EB}} f_{\text{corr}}, \tag{23}$$

with

$$f_{\text{EB}} = e^{-\beta\Sigma_{s_{\text{Pl}}}^2}, \tag{24}$$

and

$$f_{\text{corr}} = e^{3\tilde{r}\beta\tilde{\sigma}_{s_v}\tilde{\sigma}_{s_{\text{Pl}}}}, \tag{25}$$

after setting $\alpha_v = 1/3$. As expected, the Eddington bias correction increases true cluster mass at given M_{200}^{Pl}, increasing the mass bias, b (decreasing $1 - b$). A positive correlation between velocity dispersion and *Planck* mass has the opposite effect.

References

Allen, S. W., Evrard, A. E., & Mantz, A. B. 2011, ARA&A, 49, 409
Arnaud, M., Pratt, G. W., Piffaretti, R., et al. 2010, A&A, 517, A92
Battaglia, N., Leauthaud, A., Miyatake, H., et al. 2016, JCAP, 08, 013
Baxter, E. J., Keisler, R., Dodelson, S., et al. 2015, ApJ, 806, 247
Becker, M. R., & Kravtsov, A. V. 2011, ApJ, 740, 25
Beers, T. C., Flynn, K., & Gebhardt, K. 1990, AJ, 100, 32
Bleem, L. E., Stalder, B., de Haan, T., et al. 2015, ApJS, 216, 27

Bocquet, S., Saro, A., Mohr, J. J., et al. 2015, ApJ, 799, 214
Bruzual, G., & Charlot, S. 2003, MNRAS, 344, 1000
Caldwell, C. E., McCarthy, I. G., Baldry, I. K., et al. 2016, MNRAS, 462, 4117
Carlberg, R. G. 1994, ApJ, 433, 468
Carlstrom, J. E., Holder, G. P., & Reese, E. D. 2002, ARA&A, 40, 643
Colín, P., Klypin, A. A., & Kravtsov, A. V. 2000, ApJ, 539, 561
Corless, V. L., & King, L. J. 2009, MNRAS, 396, 315
de Haan, T., Benson, B. A., Bleem, L. E., et al. 2016, ApJ, 832, 95
Diemer, B., & Kravtsov, A. V. 2015, ApJ, 799, 108
Dutton, A. A., & Macciò, A. V. 2014, MNRAS, 441, 3359
Evrard, A. E., Arnault, P., Huterer, D., & Farahi, A. 2014, MNRAS, 441, 3562
Evrard, A. E., Bialek, J., Busha, M., et al. 2008, ApJ, 672, 122
Farahi, A., Evrard, A. E., Rozo, E., Rykoff, E. S., & Wechsler, R. H. 2016,
    MNRAS, 460, 3900
Guo, H., Zheng, Z., Zehavi, I., et al. 2015, MNRAS, 453, 4368
Hartley, W. G., Gazzola, L., Pearce, F. R., Kay, S. T., & Thomas, P. A. 2008,
    MNRAS, 386, 2015
Hasselfield, M., Hilton, M., Marriage, T. A., et al. 2013, JCAP, 7, 008
Heymans, C., Van Waerbeke, L., Miller, L., et al. 2012, MNRAS, 427, 146
Hildebrandt, H., Choi, A., Heymans, C., et al. 2016, MNRAS, 463, 635
Hoekstra, H., Herbonnet, R., Muzzin, A., et al. 2015, MNRAS, 449, 685
Hoekstra, H., & Jain, B. 2008, ARNPS, 58, 99
Ilic, S., Blanchard, A., & Douspis, M. 2015, A&A, 582, A79
Johnston, D. E., Sheldon, E. S., Tasitsiomi, A., et al. 2007, ApJ, 656, 27
Kay, S. T., Peel, M. W., Short, C. J., et al. 2012, MNRAS, 422, 1999
Kravtsov, A. V., Vikhlinin, A., & Nagai, D. 2006, ApJ, 650, 128
Lau, E. T., Kravtsov, A. V., & Nagai, D. 2009, ApJ, 705, 1129
Madhavacheril, M., Sehgal, N., Allison, R., et al. 2015, PhRvL, 114, 151302
Markwardt, C. B. 2009, in ASP Conf. Ser. 411, Astronomical Data Analysis
    Software and Systems XVIII, ed. D. A. Bohlender, D. Durand, & P. Dowler
    (San Francisco, CA: ASP), 251
Marriage, T. A., Acquaviva, V., Ade, P. A. R., et al. 2011, ApJ, 737, 61
Martino, R., Mazzotta, P., Bourdin, H., et al. 2014, MNRAS, 443, 2342
Mazzotta, P., Rasia, E., Moscardini, L., & Tormen, G. 2004, MNRAS, 354, 10
Mei, S., Holden, B. P., Blakeslee, J. P., et al. 2009, ApJ, 690, 42
Melin, J.-B., & Bartlett, J. G. 2015, A&A, 578, A21
Melin, J.-B., Bartlett, J. G., & Delabrouille, J. 2006, A&A, 459, 341
Meneghetti, M., Rasia, E., Merten, J., et al. 2010, A&A, 514, A93
Munari, E., Biviano, A., Borgani, S., Murante, G., & Fabjan, D. 2013,
    MNRAS, 430, 2638
Nagai, D., Kravtsov, A. V., & Vikhlinin, A. 2007, ApJ, 668, 1
Navarro, J. F., Frenk, C. S., & White, S. D. M. 1997, ApJ, 490, 493
Okabe, N., & Smith, G. P. 2016, MNRAS, 461, 3794
Penna-Lima, M., Bartlett, J. G., Rozo, E., et al. 2016, arXiv:1608.05356
Piffaretti, R., & Valdarnini, R. 2008, A&A, 491, 71

Planck Collaboration, Ade, P. A. R., Aghanim, N., et al. 2014a, A&A, 571, A20
Planck Collaboration, Ade, P. A. R., Aghanim, N., et al. 2014b, A&A, 571, A29
Planck Collaboration, Ade, P. A. R., Aghanim, N., et al. 2015, A&A, 581,
    A14
Planck Collaboration, Ade, P. A. R., Aghanim, N., et al. 2016a, A&A,
    594, A24
Planck Collaboration, Ade, P. A. R., Aghanim, N., et al. 2016b, A&A,
    594, A27
Postman, M., Coe, D., Benítez, N., et al. 2012, ApJS, 199, 25
Prada, F., Klypin, A. A., Cuesta, A. J., Betancort-Rijo, J. E., & Primack, J.
    2012, MNRAS, 423, 3018
Rasia, E., Ettori, S., Moscardini, L., et al. 2006, MNRAS, 369, 2013
Rasia, E., Lau, E. T., Borgani, S., et al. 2014, ApJ, 791, 96
Rasia, E., Meneghetti, M., Martino, R., et al. 2012, NJPh, 14, 055018
Rines, K., & Diaferio, A. 2006, AJ, 132, 1275
Rines, K., Geller, M. J., Diaferio, A., & Kurtz, M. J. 2013, ApJ, 767, 15
Rines, K. J., Geller, M. J., Diaferio, A., & Hwang, H. S. 2016, ApJ, 819, 63
Rodriguez-Gonzalvez, C., Chary, R., Muchovej, S., et al. 2017, MNRAS,
    464, 2378
Rozo, E., Bartlett, J. G., Evrard, A. E., & Rykoff, E. S. 2014a, MNRAS,
    438, 78
Rozo, E., Evrard, A. E., Rykoff, E. S., & Bartlett, J. G. 2014b, MNRAS,
    438, 62
Rozo, E., Rykoff, E. S., Bartlett, J. G., & Evrard, A. 2014c, MNRAS, 438, 49
Ruel, J., Bazin, G., Bayliss, M., et al. 2014, ApJ, 792, 45
Sayers, J., Golwala, S. R., Mantz, A. B., et al. 2016, ApJ, 832, 26
Sereno, M., Covone, G., Izzo, L., et al. 2017, arXiv:1703.06886
Sheldon, E. S., Johnston, D. E., Frieman, J. A., et al. 2004, AJ, 127,
    2544
Sifón, C., Battaglia, N., Hasselfield, M., et al. 2016, MNRAS, 461, 248
Sifón, C., Menanteau, F., Hasselfield, M., et al. 2013, ApJ, 772, 25
Simet, M., Battaglia, N., Mandelbaum, R., & Seljak, U. 2017a, MNRAS,
    466, 3663
Simet, M., McClintock, T., Mandelbaum, R., et al. 2017b, MNRAS, 466, 3103
Smith, G. P., Mazzotta, P., Okabe, N., et al. 2016, MNRAS, 456, L74
Stanek, R., Rasia, E., Evrard, A. E., Pearce, F., & Gazzola, L. 2010, ApJ,
    715, 1508
Sunyaev, R. A., & Zeldovich, Y. B. 1970, Ap&SS, 7, 3
von der Linden, A., Mantz, A., Allen, S. W., et al. 2014, MNRAS, 443, 1973
White, M., Cohn, J. D., & Smit, R. 2010, MNRAS, 408, 1818
Williams, M. J., Bureau, M., & Cappellari, M. 2010, MNRAS, 409, 1330
Wu, H.-Y., Hahn, O., Evrard, A. E., Wechsler, R. H., & Dolag, K. 2013,
    MNRAS, 436, 460
York, D. G., Adelman, J., Anderson, J. E., Jr., et al. 2000, AJ, 120, 1579
Ziparo, F., Smith, G. P., Okabe, N., et al. 2016, MNRAS, 463, 4004